Chemistry Europe
European Chemical Societies Publishing
Batteries & Supercaps

RESEARCH ARTICLE OPEN ACCESS

In Situ (Scanning) Transmission Electron Microscopy Investigation of Phase Transformation Mechanism in $LiNiO_2$ Cathode During Cycling

Ioannis Siachos[1] | Xiaodong Liu[1] | Weiqun Li[1,2] | Amirafshar Moshtaghpour[1,3] | Annalena R. Genreith-Schriever[2,4] | Tingting Yang[5] | Penghan Lu[5] | Rafal E. Dunin-Borkowski[5] | Clare P. Grey[2,4] | B. Layla Mehdi[1,2]

[1]Department of Materials, Design and Manufacturing Engineering, University of Liverpool, Liverpool, UK | [2]The Faraday Institution, Harwell Science and Innovation Campus, Didcot, UK | [3]Correlated Imaging Group, Rosalind Franklin Institute, Harwell Science and Innovation Campus, Didcot, UK | [4]Yusuf Hamied Department of Chemistry, University of Cambridge, Cambridge, UK | [5]Ernst Ruska-Centre for Microscopy and Spectroscopy with Electrons, Research Centre Juelich, Juelich, Germany

Correspondence: B. Layla Mehdi (b.l.mehdi@liverpool.ac.uk)

Received: 28 October 2025 | **Revised:** 9 February 2026 | **Accepted:** 9 February 2026

Keywords: degradation | in situ transmission electron microscopy (TEM) | lithium-ion battery | lithium nickel oxide (LNO) | Ni-rich cathodes | rock-salt formation

ABSTRACT

High Ni-content layered transition metal oxides cathodes exhibit high theoretical energy density, but their structure undergoes multiple phase transitions, which lead to reversible and even irreversible structural changes. Mechanisms leading to this degradation affect lithium transport and diffusivity, and promote oxygen loss, ultimately resulting in rock-salt formation. Here, we investigate the dynamics of the degradation mechanism of lithium nickel oxide (LNO) with the O3 stacking sequence as the starting structure, which is the most dominant structure before further delithiation. We use in situ transmission electron microscopy (TEM) to study high temporal and spatial resolution in real time of dynamic structural changes of the LNO cathode during cycling, which allows us to identify and map different phase distribution within the LNO layers during and after cycling. Combined findings from high-resolution (scanning) TEM, 4D-STEM and electron energy-loss spectroscopy reveal that the Li/Ni cation mixing layer on the pristine structure irreversibly affects the cycling efficiency by blocking the Li^+ diffusion paths. Additionally, the structural and compositional changes are accompanied by an expansion along the c-axis when the LNO is charged versus Li metal at a constant potential of 4.3 V.

1 | Introduction

Lithium ion batteries (LIBs) first became available in 1991 and have since revolutionized the consumer electronics industry. The ever-increasing need for energy storage for both industrial and household applications, such as electric vehicles, portable electronic devices, robotics, and wearable technology, has increased the interest in enhancing LIB technology by reducing the cost and improving the safety and energy density [1, 2]. The positive electrode (cathode) is the primary component of LIBs, which affects the energy density, cost, and safety of the material. The past few decades have seen increased interest in the development of suitable cathodes with the ability to accept and release Li ions smoothly. To achieve this, researchers have explored structural modifications, doping strategies, and advanced material synthesis techniques to optimize cathode performance. Despite considerable advancements, there is still room for improvement [3]. Some of the most promising lithium-containing cathodes include;

- $LiNi_{1-x-y}Mn_xCo_yO_2$ (NMC),
- $LiNi_xCo_yAl_{1-x-y}O_2$ (NCA),
- $LiCoO_2$ (LCO), and

- $LiMn_2O_4$ (LMO).

However, both LCO and $LiNi_{0.8}Co_{0.15}Al_{0.05}O_2$ (NCA) show a tendency to fast capacity fading and high cost due to the high content of cobalt [4]. LMO results in poor cycling performance due to undesirable structural changes [5]. High Ni content in NMCs ($x \geq 0.8$) leads to high power capability, but their structure tends to degrade during cycling [6]. Layered $LiNiO_2$ is one of the most promising cathode active materials (CAM), due to its low cost and higher capacity than LCO and NCA [4]. However, it suffers from structural changes during (de)lithiation, high surface reactivity, and severe oxygen evolution during cycling, raising the need for further investigation [7]. Previous studies have reported that lithium nickel oxide (LNO) undergoes phase transitions from rhombohedral H1 → monoclinic M → rhombohedral H2 → rhombohedral H3 upon delithiation [7]. The typical layered O3 structure with AB CA BC stacking sequence (and $R\bar{3}m$ space group) has a face-centered cubic oxygen framework with the alternative layers occupied by NiO_2 (TM) and Li ions (Lithium diffusion pathways) [8]. All the phases have an O3 stacking sequence, in which the "O" indicates the octahedrally coordinated intercalants (e.g. lithium) and the number denotes the three repeat units (TMO_2 slabs) per unit cell. At first, the rhombohedral $R\bar{3}m$ symmetry with trigonal structure is reduced to monoclinic C2/m, then transformed into a layered mixture of O3 and O1 (H2-H3) stacking and then further to spinel and rock-salt phase ($Fm\bar{3}m$) [9, 10]. Another study by Ohzuku et al. [11] showed that LNO involves four phase transitions for different values of x in $Li_{1-x}NiO_2$. When $0.0 \leq x \leq 0.25$ H1, for $0.25 \leq x \leq 0.55$ M, H2 for $0.55 \leq x \leq 0.75$; and a mixture of H2 + H3 for $0.75 \leq x \leq 1.0$. The transformation H2-H3 at a high state of charge (>4.15 V) results in the poorest performance in terms of intrinsic stability of LNO as it is accompanied by a sudden collapse of the structure along the crystallographic c-axis [7]. The difficulties of LNO cathodes can even occur before cycling, due to the instability of Ni^{2+} ions, which tend to occupy lithium sites, exhibiting antisite defects and leading to the blocking of channels that hinder the diffusion of lithium. The instability of Ni^{2+} ions arises from their high mobility and tendency to migrate under certain synthesis and storage conditions, particularly when exposed to elevated temperatures or insufficiently controlled oxygen partial pressures during material preparation. Furthermore, this issue can be attributed to the similar ionic radii of the Ni^{2+} (0.69 Å) and Li^+ (0.76 Å) [12]. This phenomenon is confirmed by many other groups as well, which showed a small percentage (≤5%) of residual Ni^{2+} in the Li layer [12, 13]. This leads to stoichiometric issues that narrow the stability window of LNO, creating a strong oxidation environment to stabilize the Ni^{3+}. Thus, controlling the stoichiometry remains a major challenge; due to the instability of LNO at high temperatures and/or excessive cycling, where the loss of Li (or rather Li_2O) leads to material decomposition [14, 15], and that decomposition reaction can be written as:

$$LiNiO_2 \rightarrow \frac{1}{1+z} Li_{1-z}Ni_{1+z}O_2 + Li_2O + \frac{z}{2(1+z)} O_2$$

Furthermore, density functional theory calculations have been implemented to create ground state phase diagrams for the $LiNiO_2$–NiO_2–NiO system. This scheme (Figure 1a) illustrates a triangle where the three vertices illustrate 100% Li ($LiNiO_2$), 100% Li vacancies (NiO_2), and 100% Ni (NiO). Black circles within this ternary phase diagram indicate stable phases that have already been reported, and lines indicate known phase transitions [16–18]. As Li concentration decreases, the spinel phase appears, which is the only stable phase identified in that region during delithiation. Further oxygen loss and Ni densification lead to the final rock-salt formation. This article aims to examine the intermediate disordered structures or the unidentified *meta*-stable phases, red circles, that are present inside this phase diagram via in situ transmission electron microscopy (TEM) technique, as well as 4D-scanning TEM (STEM) to map the phase distribution across the LNO cathode during in situ TEM cycling. These intermediate phases emerge during delithiation, forming between the layered and rocksalt stable structures. Their presence influences lithium diffusion pathways and the overall cycling stability of the cathode [19].

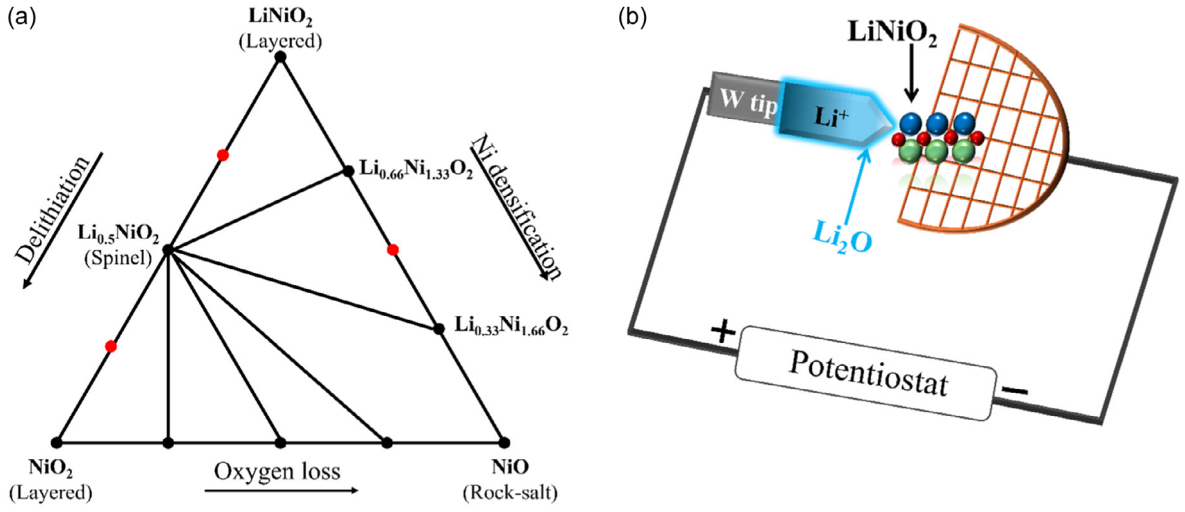

FIGURE 1 | (a) Ground state Li–Ni-vacancy ternary phase diagram for the $LiNiO_2$–NiO_2–NiO system. Black circles with solid lines represent the stable phases with the identified phase transitions, respectively. Red circles illustrate the unidentified *meta*-stable phases. (b) Schematic illustration of the in situ open-cell TEM configuration with a solid metal oxide electrolyte (Li metal/Li_2O) and $LiNiO_2$ as the positive electrode.

1.1 | In Situ TEM Open-Cell Studies

In recent years, great progress has been made in the development of new in situ and operando techniques that allow for real time observation of chemical and structural changes in LIBs during cycling. One of the most widely used techniques is an in situ open-cell TEM that can provide real-time monitoring of a solid-state electrochemical process, and interfacial reactions between the electrode and the solid electrolyte, ultimately leading to phase changes [20, 21]. In situ open-cell TEM provides a solid-state nanoscale platform to drive Li^+ extraction reactions under an applied potential, enabling direct observation of structural and chemical changes in electrode materials. This configuration does not reproduce the operating conditions of a commercial lithium-ion battery but instead focuses on the intrinsic delithiation-induced phase transformations at the single-particle level. This technique enables the study of lithium-ion (de)intercalation, phase transitions, and structural evolution of CAMs, providing insights into the discrepancies between the simulation and experimental results, as well as the degradation mechanisms and dynamic phase changes that occur during cycling [22, 23]. Wang et al. and Huang et al. had pioneered the concept of an in situ TEM cell based on their first use of open cell to study energy storage materials including Si, Ge, SnO_2, ZnO, graphene, and carbon nanotubes, providing groundbreaking insights into their lithiation/delithiation mechanisms and structural evolution during electrochemical cycling [22, 24, 25]. Due to the high vacuum inside TEM, open-cell configuration cannot incorporate battery liquid electrolyte and instead uses ionic liquid electrolyte or metal oxide as solid-state electrolyte, required for in situ electrochemical experiments to drive the electrochemical reaction inside the TEM [20]. Li metal will be partially oxidized, and a thin layer of lithium oxide will cover the surface to play the role of a solid electrolyte to create a Li^+/Li_2O mixture, which is used as an anode and solid state electrolyte versus a cathode material [26]. By applying positive potential between the cathode and the Li metal, lithium ions will be attracted from the positive electrode into the lithium tip. Wang et al. [10] investigated in depth dynamic changes in rechargeable battery materials through an in situ TEM open-cell approach. Their main focus was the direct observation of the lithium ions insertion and removal impact on nanowire electrodes (mostly Si). The authors addressed the gap between real-world battery operation and atomic-level studies by linking electrochemical data with material transformations such as lithium dendrite formation, phase transformations, and the development of the solid electrolyte interphase (SEI). Using in situ open-cell TEM presents several challenges that researchers have yet to fully overcome. One issue is the lack of multiple contact points between the two sources (electrode/electrolyte) and different charge transfer resistances [22, 27]. Another challenge of performing in situ TEM experiments is beam damage, which can lead to alterations in the surface or bulk structure of the material by triggering side reactions [28]. Studies have shown that the electron beam dose can have a profound effect on the in situ TEM experiments and can accelerate or decelerate the lithium intercalation process by decomposing lithium oxide (Li_2O) to drive Li at nearby electrodes [29]. Despite these challenges, in situ TEM remains an indispensable technique for studying dynamic processes in battery materials at the atomic scale, as its unique capabilities provide invaluable insights that cannot be obtained using other methods.

1.2 | Methodologies Followed for Investigating LNO Degradation

In this work, we utilize in situ TEM open-cell approach to study degradation mechanisms of the $LiNiO_2$ cathodes during delithiation process to understand the phase transition in real time. Figure 1b illustrates the experimental setup, where LNO nanoparticles are attached to a half-holey carbon copper grid, while lithium metal is positioned on a tungsten needle mounted inside the Ar-filled glovebox. Delithiation experiments were performed by applying a constant positive bias of +4.3 V to the $LiNiO_2$ (LNO) particle, while the Li/Li_2O counter electrode was electrically grounded. The experiments were conducted using an in situ open-cell TEM configuration, in which metallic Li is partially converted to a thin native Li_2O layer that acts as a solid-state electrolyte, enabling Li^+ transport under an applied electric field. Upon application of the positive bias, Li^+ ions are extracted from the LNO particle and migrate through the Li_2O layer toward the Li electrode. Although the open-cell configuration does not replicate a full liquid-electrolyte battery environment, this approach has been widely used to probe lithiation and delithiation mechanisms in Li- and Na-ion battery materials at the nanoscale, as demonstrated in prior in situ TEM studies. The applied bias of +4.3 V was selected because it corresponds to the upper cut-off voltage of $LiNiO_2$ versus Li/Li^+, associated with the H2 → H3 phase transition regime, where pronounced c-axis expansion and the onset of structural instability are known to occur. This voltage window is therefore particularly relevant for directly observing degradation mechanisms and irreversible phase transformations in LNO, contributing to a deeper understanding of its structural evolution and lithiation kinetics during cycling. STEM is a powerful tool to measure the electronic structure and bonding in terms of mechanical and transport properties of a LIB material. Dark field (DF) and bright field (BF) STEM imaging techniques are advantageous for performing atomic high-resolution analysis. However, they are generally sensitive to lower atomic number (Z) elements, such as Li and O [30]. Therefore, we implement an electron energy loss spectroscopy (EELS) technique to examine the changes in the valence state of nickel in the LNO cathode particle after delithiation. This work investigates delithiation mechanisms in $LiNiO_2$, focusing on oxygen loss, oxygen vacancies, and their correlation with the Ni valence state using EELS data. Recent studies, such as that by Genreith-Schriever et al. [31], highlight the critical role of oxygen hole formation and oxygen redox activity in structural stability. Building on this framework, the degradation pathway summarized schematically in Figure 2 highlights how oxygen hole depletion, oxygen vacancy formation, and the accompanying reduction of Ni collectively drive the transition from the layered structure toward disordered and rock-salt phases. Establishing a direct link between oxygen holes, oxygen vacancies, and Ni valence states is therefore central to understanding the irreversible structural evolution of LNO during high voltage delithiation. To investigate these changes, the spectra were collected from various points of the sample from the surface to bulk of the delithiated particle, focusing on the Li-K edges, Ni-M, L edges, and the O-K edges.

First, we focused on characterization of nickel-$M_{2,3}$ edges and lithium-K edge in the low-loss region of the spectrum (near to the zero-loss peak). However, as lithium is located in the low-loss region of the spectrum, this edge might be subject to high delocalization and the overlapping of Ni-$M_{2,3}$ signals, which makes

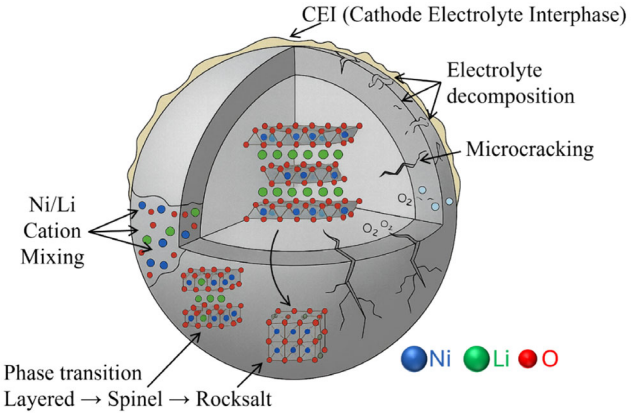

FIGURE 2 | Schematic summary of the degradation pathway in $LiNiO_2$ during delithiation.

the detection of the lithium more complicated [32, 33]. To overcome this, we use high resolved EELS and reference spectrums of Ni^{2+} and Ni^{3+}, aiming for the direct comparison with the experimental results to enhance the valence state calculations. Furthermore, we focused on the O prepeak and the O-K edge to track structural changes in oxygen bonding and oxygen redox reactions associated with the presence of different oxygen environments within the LNO cathode [34, 35]. In the parallel nickel-$L_{2,3}$ edges are important for the examination of nickel's electronic structure and oxidation state, providing insights into the interactions between nickel and oxygen within the particle and helping to monitor electronic changes in nickel, which is crucial for understanding degradation mechanisms. In complex materials like LNO, particularly after delithiation, the most critical thing is to identify all the different phases and structures within the cathode. For this reason, we employ a crystal orientation mapping (COM) [36–38] and adopt a technique introduced in [39]. This method involved acquiring 2D convergent beam diffraction (CBED) patterns for every position of a focused electron beam, resulting in a 4D-STEM dataset. Those CBED patterns were recorded utilizing a fast pixelated detector, simultaneously allowing us to acquire HAADF images from a localized structure, which made it easier to characterize the sample in detail. The underlying idea in COM is that the CBED patterns of crystalline materials contain Bragg peaks with spacing inversely proportional to the spacing of atomic planes. As instructed in [39], the Bragg spots at every probe position were identified using a template matching procedure. Given the structural data of a reference crystal, an orientation plan was created, which was then used to find the best orientation match for each probe position. Since our sample contained multiple phases, we performed this process for each reference crystal structure. Phase identification was achieved through a multistep COM analysis. Distinct COM experiments were conducted on three reference materials: pristine LNO, Li/Ni disordered phase $Li_{1-x}Ni_xO_2$, and rocksalt NiO. Each COM experiment yielded unique orientation maps characteristic of the respective phase. By extracting the most distinctive features from each orientation map, we assigned a unique color (RGB) to represent each phase. This color-coding scheme enabled the identification and mapping of the various phases and their intermediates within the LNO cathode material during degradation. Electron ptychography is an alternative approach that uses 4D-STEM data for obtaining the relative phase shift between the light and heavy elements in a sample with atomic resolution. An example of such a method made it possible to detect the oxygen distortion and precisely identify oxygen inside the structure, with requirements of a thin sample to visualize such atoms [40, 41].

In this work, we demonstrate direct observation of the time-resolved phase transformation of LNO at the nanoscale using insitu open-cell TEM, enabling analysis of a single primary particle during lithiation and delithiation while accessing the intrinsic electrochemical reaction pathways of the material.

2 | Results and Discussion

This study explores the phase transformation mechanism of the high energy density $LiNiO_2$ cathode. In situ TEM open-cell approach was initially utilized to observe the real time electrochemical changes in the LNO structure during delithiation at 4.3 V. Then, 4D-STEM was used to map phase evolution and identify transitions in the $LiNiO_2$–NiO_2–NiO ternary phase diagram. Furthermore, EELS was implemented to address oxygen vacancies and valence states and how the reduction of nickel and oxygen loss during delithiation impacts the battery performance. These combination of techniques outline the clear picture of structural and chemical changes involved in LNO performance and help us explore ways to improve the stability and efficiency of Ni-rich cathodes.

The SEM images in Figure S1 show the overall morphology of the LNO nanoparticles with sizes ranging from 200 to 800 nm. Energy-dispersive X-ray spectroscopy (EDS) maps (Figure S2) indicate the uniform element distribution for the LNO particles. Atomically resolved (S)TEM images were acquired to confirm the layered structure with the O3 stacking sequence of the pristine LNO material (Figure 3); Figure 3a demonstrates the distinct atomic planes of the layered pristine sample, the layers of the transition metal (NiO_2) and the lithium channels. The O3 stacking regularity was observed in Figure 3b, with a blue color assigned for nickel ions, red for oxygen, and green for lithium ions. High-resolution TEM image (capture in Figure S3a) illustrates clearly the layered structure of the pristine LNO with distinct atomic planes of the (003) facet. The line profile is used to calculate the d-spacing of that facet, which is 4.8 Å (Figure S3c) and refers to the distance between the adjacent NiO_2 layers, which are separated by channels that include lithium ions (Li^+). The spacing between these layers represents the width of the channels, which allows the Li^+ diffusion during cycling. It should be noted that such a value is higher than the theoretical d-spacing of layered LNO along the (003) plane most probably due to the slight drift of the specimen or the synthesis approach used [43]. When the image was taken along the [110] zone axis, different signals of the (006) (2.4 Å) and (101) (2.53 Å) appeared on the fast Fourier transform (FFT) image (Figure S3b). However, a closer look at the surface of LNO in Figure 3a suggests the presence of a Li/Ni disordering layer around 5 nm thick from the synthesis of the CAM (denoted by the red dashed box). This disordered layer exhibits a native rocksalt-like structure, where a fraction of Ni^{2+} ions substitute Li^+ sites, leading to cation disorder in both sublattices (i.e., Ni occupying Li sites and Li occasionally found in transition metal layers). The thickness of this layer is not perfectly uniform, varying slightly between

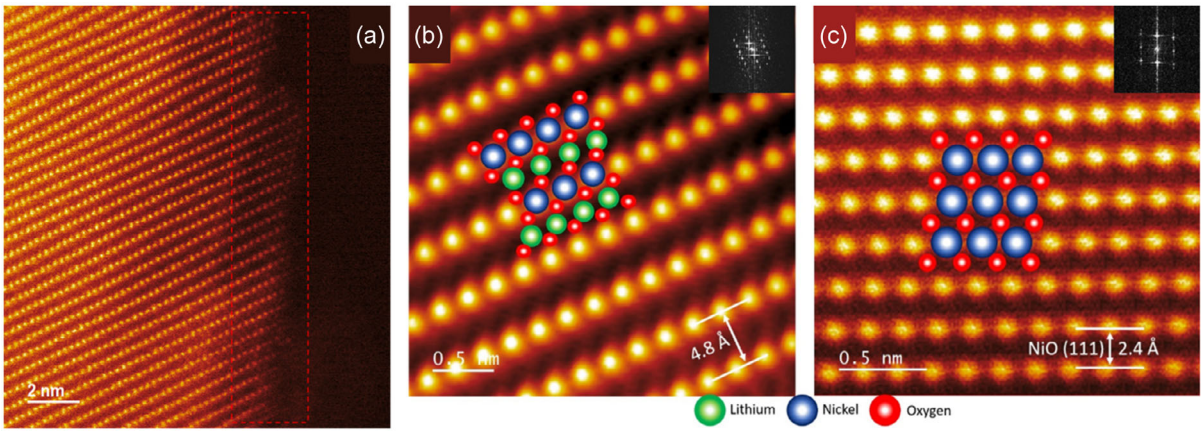

FIGURE 3 | High resolution dark field STEM images of (a) pristine layered LNO, (b) higher magnification image showing the O3 stacking sequence and R$\bar{3}$m space group, and (c) pure NiO phase, at the [211] zone axis, shows the atomic planes of (111) NiO with Fm$\bar{3}$m space group, which occurred after the delithiation. Reproduced from Ref. [42] with permission from Oxford University Press.

4–6 nm, depending on local synthesis conditions and surface termination. The shape of the disordered layer tends to follow the natural particle morphology. According to literature, even under a very well-controlled environment, there is at least 2%–3% of residual Ni^{2+} in the Li channels, creating a Ni/Li cation disorder layer that hinders the smooth flow of Li ions, affecting the cycling performance [44–46]. Recent studies have explored low-temperature ion-exchange synthesis, such as from $NaNiO_2$ to $LiNiO_2$, as an effective approach to minimize lithium loss and reduce antisite defects in layered cathode materials [47]. Figure 3c reveals the transformed structure of the cathode material into the rock-salt phase of NiO after delithiation, achieved via an in situ TEM open-cell approach when a positive bias of 4.3 V was applied. This observation indicates the significant rearrangement of the rock-salt phase, where the Ni and O atoms are located in such positions that the resulting crystalline structure is usually much denser and more uniformly packed than that of the pristine layered one.

Among all phases, the H2 to H3 transformation results in poor structural stability, especially while operating at high voltages [48]. We have examined structural and compositional changes of the stoichiometric $LiNiO_2$ when a positive voltage of 4.3 V is applied in the LNO particle by the implementation of an in situ open-cell TEM approach. The understanding of the phase transition impact during Li de-intercalation has been pointed out in Figure 4, where the series of the first delithiation process is demonstrated. This resulted in an expansion of the particle at about 26% projected particle expansion over 70 s as shown in Movie S1 (Supplementary Information), which can be described as a significant change in the lattice parameters during the structural transformation. Due to the large volume change during high voltage cycling, concurrent rock-salt transformation is identified [49]. A series of low magnification TEM images (Figure 4a–d) show the lattice expansion and the change in the initial LNO structure. Movie S2 (Supplementary Information) shows the expansion of another LNO particle at about 30% projected particle expansion when it was charged at a constant voltage of 4.3 V (Figure 4e–h). The reaction appears at the first 10 s of charging with changes in the contrast of the particle marked with the orange dashed line (Figure 4f). Furthermore, the expansion started at the 27 s under the positive bias (Figure 4g) and continued till the particle has been transformed at about 60 s (Figure 4h). A comparison between the pristine and the delithiated particles can be observed through a series of HRTEM images after the 108 s of constant charging at 4.3 V. Figure 4i–l shows a high magnification time-resolved in situ series of TEM images of an LNO particle, shown in the in situ Movie S3 (Supplementary Information) upon charging at a positive bias of 4.3 V.

As expected, there is a volume change during 1st delithiation, where the expansion starts at the first 30 s of the Li removal process, the transition is also confirmed by the FFT shown in Figure 4j where apart of the layered structure's reflection one more peak appears (indicated by the red arrow), which shows the transition of Ni in the Li slab layer. The main (003) planes are still visible even after 1 min of delithiation; however, the FFT signal becomes weaker (Figure 4k). At this point, the phase transition of the LNO particle has already started taking place, where the initial layered structure of $LiNiO_2$ is transforming into NiO-rich areas after the Li removal and the oxygen loss. The final frame after 110 s shows the presence of two different phases in the delithiated region of the particle, as the FFT indicated the presence of two polycrystalline structures (Figure 4l), with d-spacings of 2.4 Å (green) and 2.1 Å (red), respectively. The pristine layered structure with the distinct atomic planes of (003) with 4.8 Å d-spacing transformed into NiO with the lattice planes of (200) found at 2.1 Å. That result is explained as the distance of the Ni- Ni* slab layer where the one Ni is at the starting octahedra position while the second Ni* is found at the octahedra position of Li vacancy [6]. In order to gain a more detailed picture of the phase evolution we utilized 4D-STEM, not only to identify the various phases (stable and metastable) but also to visualize how far the delithiation had progressed, where the rock-salt phase appeared to be taking place and investigate whether the nanoparticle formation at the LNO's surface consists of pure NiO species clearly seen in Figure 4l inset or if residual lithium remains as lithium oxide (Li_2O) and lithium peroxide (Li_2O_2) as phase-separated compounds, suggested by Wang et al. [48]. Next, we investigated the dynamic process that occurred in the LNO upon delithiation. Movie S4 (Supplementary Information) revealed that during charging at 4.3 V LNO particle undergoes a phase transition in the first 15 s. The reaction appears as a wave-like propagation of lithium concentration that moves across the

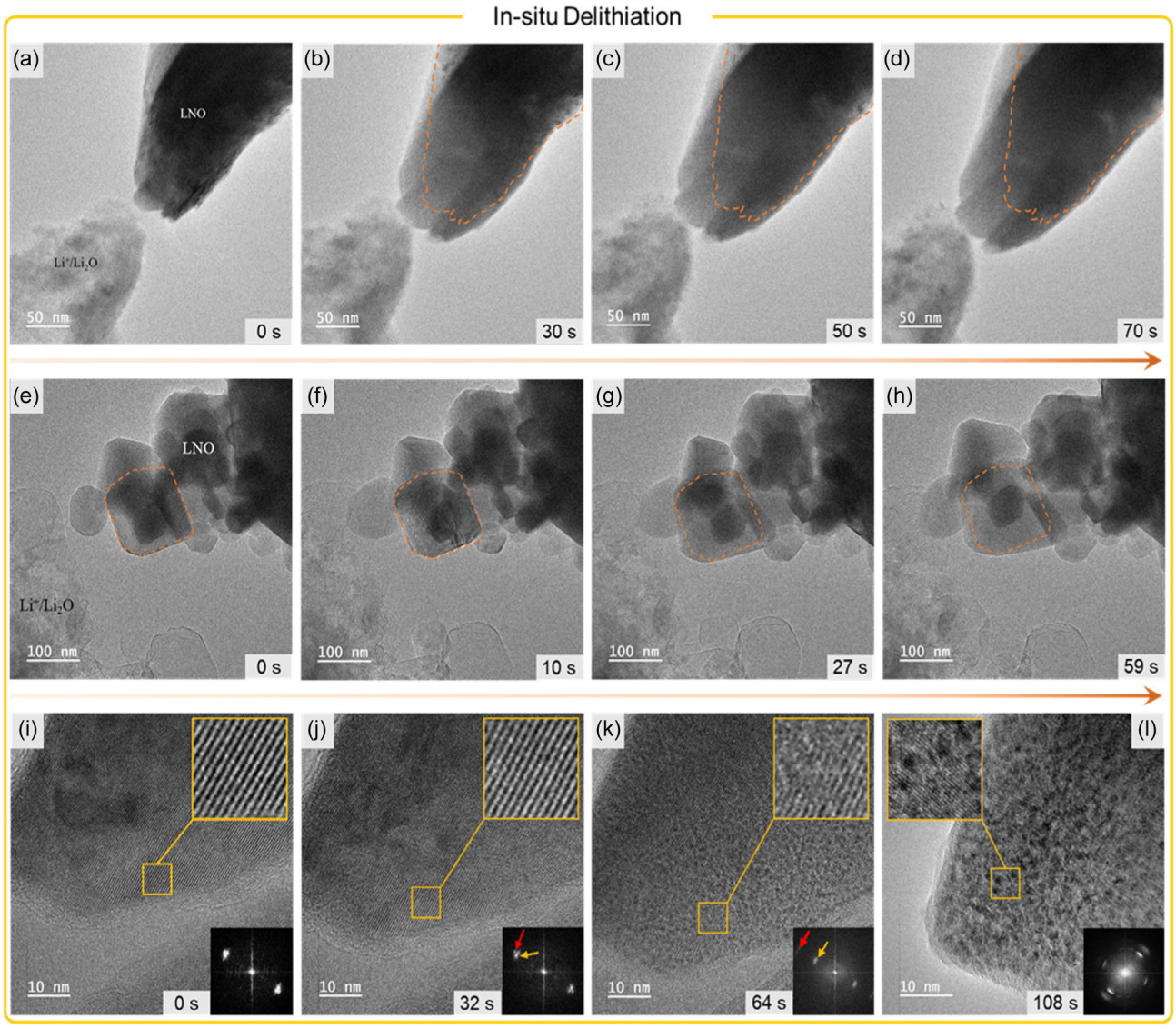

FIGURE 4 | (a) Low magnification TEM image of Lithium metal and LNO before delithiation. (b–d) Time series of delithiation of LNO at 30, 50, and 70 s, respectively, highlighting an expansion of ∼26% increase in projected particle dimension measured from TEM images. Reproduced from Ref. [42] with permission from Oxford University Press. (e–h) Time series during delithiation of a second LNO particle at low magnification illustrating a total projected particle expansion of ∼30% after 59 s of charging at 4.3 V. (i–l) Series of high magnification TEM images before delithiation (i), after 32 s (j), after 64 s (k), and after 108 s (l), at constant charging at 4.3 V, with FFT patterns showing initially the distinct (003) atomic planes (orange arrow) but as the reaction propagated another phase appeared (red arrow) to finally form a polycrystalline pattern of NiO rock-salt phases. Inset into these images are the FFTs and the zoomed-in images of atomic planes of the layered and rock-salt structures present within the material.

positive electrode from the surface of LNO toward the core of the cathode particle. This reaction forms a lithium-poor phase starting from the edges and then the whole region has undergone reaction; this phase boundary movement is aligned with previously reported mechanisms of "shrinking-core" and "intercalation wave" [50, 51]. The shrinking core mechanism is described as lithium ions eliminated during discharging, which represents the steady migration of a reaction front or interface within the particle. This mechanism causes the particles' lithiated center to gradually shrink as the lithium is extracted from the surface inward [52]. To verify that this phase-front propagation arises from voltage-driven lithium extraction rather than from physical contact or electron-beam exposure, control experiments were performed in which $LiNiO_2$ particles were brought into direct contact with Li/Li_2O in the absence of an applied electrical bias. Under these conditions, no lattice expansion, phase transition, or rock-salt formation was observed, confirming that the dynamic evolution reported here is attributed to electrochemical delithiation (Figure S4).

An important challenge in this experiment is to understand the structural changes that the LNO particle undergoes during the delithiation process and identifying these phases. Simulated data based on the concept of the phase diagram has demonstrated all the possible phases the LNO can have during the Li removal process, consisting of $LiNiO_2$, intermediate $Li_{1-x}Ni_xO_2$ and rock-salt NiO [53]. This knowledge is critical to optimize the stability and performance of LNO. In addressing this crucial issue, we implemented the comprehensive analysis of 4D-STEM phase mapping and the corresponding CBED patterns as presented in Figure 5. Figure 5a illustrates a detailed phase map with distinct colored

regions, where each color represents various structural transformations as indicated by the triangular phase diagram. The green regions as appeared in the phase map show the pristine layered LNO structure. The CBED patterns from these regions with their crystal diffraction patterns in Figure 5b show characteristic (003) and (006) reflections of the layered structure with R$\bar{3}$m space group (hexagonal symmetry). As delithiation progresses, the phase map (blue regions) reveals an increasing degree of Ni/Li disorder, where both surface-driven and bulk-driven mechanisms contribute to the transformation, but the most dominant, especially at the early stage, are surface processes (Ni diffusion and oxygen loss), particularly near the reaction front. The CBED patterns from the blue regions (Figure 5c) show a consistent rearrangement with Ni ions occupying the vacant Li channels, altering the crystal structure. The surface-driven Ni migration acts as the main propagation mechanism, appearing in a wave-like manner that leaves behind lithium-poor areas, where the Ni/Li disordered phase thus emerges as an intermediate structure before full transformation into the rock-salt phase. Afterward, the purple regions with their electron diffraction patterns (Figure 5d) illustrate the continuation of the intermediate phase (Ni/Li disordered) along with the appearance of a secondary phase at 1.95 Å. This phase signifies the initial stages of further structural rearrangement as the reaction front proceeds. The formation of the secondary phases can also be attributed to the loss of oxygen atoms at that point. The reaction of oxygen loss is one of the main reasons which significantly affects the structural integrity and phase composition of the LNO [54]. Pink regions appear as we move closer to the reaction front, where the LNO exhibits polycrystallinity. Figure 5e shows the CBED patterns attributed to the pink regions, where strong reflections from NiO crystals [(111), (200), and (220)] are presented. This polycrystalline phase illustrates significant structural changes as the reaction front advances. Lastly, red regions are the most dominant color at the reaction front, where the structure has been transformed into polycrystalline NiO. The CBED patterns (shown in Figure 5f) highlight the same major reflections from the (111), (200), and (220) atomic planes. This results in the peak of the delithiation reaction of LNO, where the original pristine structure has been extensively converted to form polycrystalline NiO. While the ternary phase diagram in Figure 1a defines the thermodynamically stable phases of the Li–Ni–O system, the 4D-STEM data directly resolve a series of nonequilibrium, metastable intermediates that arise during deep delithiation. These intermediates are not ground-state phases, but they represent kinetically accessible transformation pathways under high-voltage

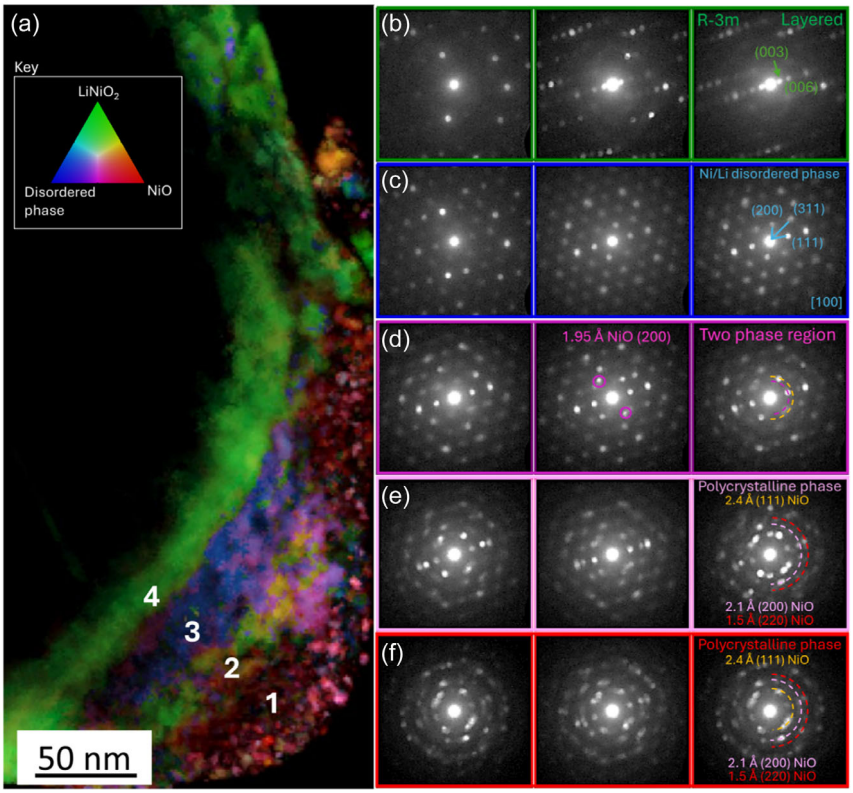

FIGURE 5 | (a) Phase mapping of the LNO particle after in situ delithiation from the 4D-STEM dataset. Different colors representing various phases indicated by the triangle at the top, corresponding to the transformation of LNO upon Li removal: green for the pristine layered structure, blue for the Ni/Li disordered phase, and red for the reaction front where NiO crystals dominate. (b) CBED patterns taken from the green regions, where the structure maintains its pristine form (layered), with the main reflections of (003) and (006). (c) CBED patterns from the blue regions, representing the reaction's furthest point where the phase has transitioned to a Ni/Li disordered state, with some Ni ions occupying the Li sites. (d) CBED patterns from the purple regions, showing the Ni/Li disordered phase with the emergence of a second phase. The appearance of new reflections indicates the transition toward the pink region. (e) CBED patterns from the pink region, where polycrystallinity has developed near the reaction front. Major reflections come from NiO crystals, with (111) and other planes visible. (f) CBED patterns from the red regions, representing the reaction front where the structure is predominantly polycrystalline NiO. Reflections from (200), (111), and (220) planes are marked.

conditions. Specifically, the blue regions in Figure 5 correspond to a Ni/Li-disordered layered phase formed by kinetically driven Ni migration into Li layers; the purple regions indicate oxygen-deficient layered variants stabilized by vacancy formation, evidenced by the emergence of new reflections (~1.95 Å); and the pink regions represent early-stage rock-salt nanodomains associated with surface reconstruction. Together, these observations demonstrate that the role of Figure 1a is to provide thermodynamic anchors, while the 4D-STEM data reveal the metastable pathways connecting them during operando delithiation.

EELS was conducted to provide chemical and electronic insights; to help us distinguish the various phases as seen in the delithiated LNO particle (Figure 5a). The goal is to understand how the oxygen bonding, vacancies and nickel oxidation state impact the performance of the LNO. The EELS spectra of $LiNiO_2$ taken before and after delithiation in Figure 6 specifically focus on the O K-edge and Ni-L edges to complement our understanding of local phase changes after cycling. Figure 6a shows the line profile of EELS spectra (1 → 4) taken at the O K-edge, which illustrates distinct changes between the three different distinct regions: green, blue, and red. The first major peak at 529.55 eV is identified as oxygen K-edge prepeak, which originates from transitions from O 1s to unoccupied O 2p states that are strongly hybridized with Ni 3d orbitals, and therefore directly reflects the presence of oxygen holes, the degree of Ni–O covalency, the specific number of oxygen hole formation and more details regarding oxygen redox activity.

As delithiation progresses, a simultaneous fading of the O-K edge prepeak and a shift of the Ni-L_3 edge toward lower energy are observed. The Ni-L_3 shift, accompanied by an increase in the L_3/L_2 intensity ratio, is consistent with the reduction of Ni^{3+} to Ni^{2+}. Importantly, in the EELS line scans acquired across the reaction front, the disappearance of the O-K edge prepeak and the Ni-L_3 energy shift occur at the same spatial locations, with no evidence of one occurring before the other. O-K edge (second major) at ~ 540 eV results from electron transitions from O-1s core level to unoccupied O-2p orbitals. The intensity of the first peak helps us to estimate the number of unoccupied Ni-3d orbitals per oxygen atom: 1.5 (three orbitals for two oxygen atoms) in $LiNiO_2$ (Ni^{3+}: d7); due to the covalent bonding between O-2p and Ni-3d orbitals, which takes place at the first peak [55, 56]. The experimental spectrum (4) taken from the bulk of the particle is aligned with the reference sample (3+) in terms of the sharpness and the activation energy (859 eV) of both peaks, suggesting that the reaction has not reached that region. The prepeak on the green region is 11.75 eV away from the O peak; that distance becomes smaller as the O-K edge signal shifts toward lower activation energies. This phenomenon can be explained by the oxidation and reduction reactions that the LNO undergoes as the Li is removed from that region and the further oxygen loss. Furthermore, inside the blue box in Figure 6a, we can observe that this prepeak has started disappearing as the spectrum gets closer to the reaction front (4 → 1), proposing that the sample has become rock-salt. The fading away of the O-K pre edge was previously reported as an incident that frequently occurs in rock-salt structures, which is attributed to the full reduction of O to O^{2-}, meaning there are no electron holes on O and, consequently, no prepeak. This phenomenon is also associated with the formation of oxygen vacancies, changes in the atomic structure, such as the migration of transition metals, and the reduction of these metals, leading to the formation of ionic bonding [57–59]. Furthermore, Figure 6b illustrates Ni-$L_{2,3}$ peaks of the pristine LNO consisting of two major peaks at 859 eV and 876.25 eV for the green region respectively. The local electronic structure of the nickel atom, e.g. oxidation number, spin state, and coordination number affect the shape of the $L_{2,3}$ edge due to the localization of Ni-3d orbitals on a Ni atom. The two peaks are associated with transitions from $2p_{3/2}$ to unoccupied 3d states ($3d_{3/2}$ and $3d_{5/2}$) for the L_3 edge and transitions from $2p_{1/2}$ to unoccupied 3d states ($3d_{3/2}$) for the L_2 edge [60, 61]. As the EELS line scans the particle from bulk to the surface a noticeable fact is that the L_3 peak appears with an energy shift at about 1.25 eV (from 859–857.75 eV) toward lower energy levels, confirming that Ni ions are reduced during the delithiation process, aligned with the findings of Weatherup et al. who demonstrated that Ni ions near the surface of LNO undergo a similar reduction to Ni^{2+}, forming a reduced surface layer (RSL) approximately 200 nm thick. This reduction was accompanied by the formation of molecular O_2 near the surface [62]. The results calculated from the intensity ratio of these two peaks suggest that the ground state of the nickel atoms is Ni^{3+} with a low spin state in LNO. The intensity ratio between the L_3 and L_2 peaks of Ni are highly reliant upon the d-band occupancy and thus of the elemental transition state [63–65]. For the most accurate calculation of the valence state of Ni, the intensities of the L_3 and L_2 peaks must be determined reliably, and numerous methods have been proposed throughout the years [66, 67]. Figure S5 represents an EELS spectrum taken at the low loss region, close to the zero-loss peak. Line profiles from the surface (1) to bulk (4) illustrate the behavior of the Li-K edge peak (at 63 eV) and another major peak at 71 eV, which is suggested as the Ni-$M_{2,3}$ edges has much weaker spin–orbit coupling on Ni-3p orbitals than on Ni-2p is the reason why a clear separation between Ni-M_2 and M_3 cannot be observed [55]. As expected, the

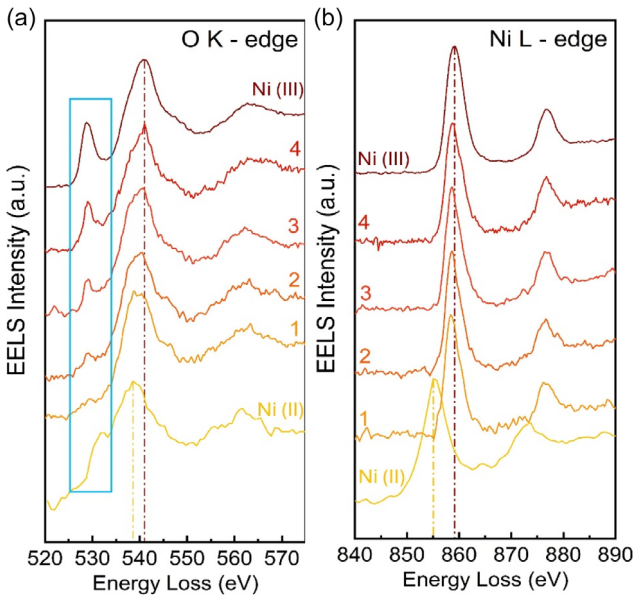

FIGURE 6 | (a) Shows the O-K edges, the blue box highlights the oxygen pre-edge peaks. (b) Shows the Ni L-edges EELS spectra in the core loss region. Reference spectra for oxidation states Ni III and Ni II for a comparative analysis. The experimental spectra originated from the bulk material (labeled as '4'), intermediate regions (labeled as '2' and '3'), and the surface region (labeled as '1').

signal from the Li K-edge becomes weaker toward the surface. Figure S6 shows measured ratios between the L_3, L_2 Ni peaks from four different samples, three references (NiO for Ni II, Ni from pristine LNO for Ni III, and NiO_2 for Ni IV), and the spectrum taken from the surface (red) region of the $LiNiO_2$ cathode, confirming the reduction in the valence state of Ni to the final phase of NiO. This reduction of Ni results demonstrates an increase intensity ratio between the L_3 and L_2, due to the increased population of 3d electrons enhancing the L_3 absorption intensity more than the L_2, also confirmed by other groups [68–71].

3 | Conclusions

In summary, degradation of $LiNiO_2$ during cycling was characterized by an advanced in situ open-cell TEM approach, 4D-STEM, and EELS spectroscopy, to examine the phase transformation mechanisms in Ni-rich cathodes. Our comprehensive use of the in situ TEM technique allows for the direct observation of real time structural and compositional changes, attributed to phase transitions withing the LNO particle. While previous studies have relied only on in situ TEM data [10, 41], our comprehensive implementation of in situ open-cell TEM, 4D-STEM, and EELS provides a more detailed picture of the dynamic changes of the LNO cathode during battery operation. The pristine layered structure of LNO was well investigated, as to how the Li/Ni disordered layer affects the paths of both Ni and Li during cycling and the phase transitions. This set of experiments showed interesting results in the lattice parameters with the changes in d-spacing from 4.8 to 2.1 Å, indicating lattice expansion along the c-axis and volume change upon high voltage charge (4.3 V) of about 20%–30% after the second lithium deintercalation experiments took place. This reported expansion corresponds to the change in projected particle dimensions measured from time-resolved TEM images, rather than to crystallographic lattice expansion alone. In the in situ open-cell nanoscale configuration, delithiation proceeds under conditions that promote deep structural reconstruction, including a high surface-to-volume ratio and direct Li/Li_2O contact. At high states of delithiation, $LiNiO_2$ evolves beyond the H3 phase toward oxygen-deficient and ultimately NiO-type rock-salt structures, consistent with high-voltage surface reconstruction reported for Ni-rich layered oxides. This quantified lattice expansion along the c-axis provided a thorough understanding of the mechanical stress and structural degradation of the LNO cathode. An irreversible rock-salt transformation was observed at the end of the delithiation process, but no porous formation was recorded. This irreversible change is also justified by the few nanometers-thick disordering layer on the surface of the pristine material which blocks the Li diffusion path. This work represents an important approach in studying the degradation mechanisms of LIBs by utilizing 4D-STEM measurements for phase identification mapping of both light and heavy elements, which features are necessary for the detection and analysis of lithium, especially in materials like LNO, where the Li identification is particularly challenging. We utilized 4D-STEM for a detailed phase mapping analysis to capture effectively the structural changes of the LNO cathode. This allowed the location of different layers, including layered pristine, Ni/Li disordered phase, and polycrystalline areas rich in rock-salt NiO nanoparticles, and thus the delivery of a phase diagram of the LNO during cycling. By cross-correlating different techniques with the theoretical models, therein, the present work not only illustrates the intrinsic complexity of LNO behavior during delithiation but also justifies the need for advanced imaging techniques to unravel electrochemical pathways of next-generation energy storage materials. The EELS spectrum verifies the electron valence state of the pristine LNO. To complete the investigation, we used time-resolved EELS to provide us with direct observation of oxygen loss, Li removal, and Ni valence state at the rock-salt phase by comparing the elemental ionization edges. The delithiated particle was examined and the changes in the signal peaks were observed by investigating the valence state of Ni in the rock-salt formation. This work showed important insights into the phase dynamics, structural features, and chemical heterogeneity within the LNO particle by thorough EELS spectral analysis from the low-loss and core-loss areas. These insights are critical for optimizing the cathode design and performance in battery applications. In summary, this study greatly advances the fundamental understanding of the degradation process and changes in structure in Ni-rich cathodes during cycling, emphasizing the importance of a comprehensive understanding of phase transition, cation mixing effects, and lattice expansion, which is crucial in the rational design of more stable and efficient cathode materials for advancing next-generation LIBs.

4 | Materials and Characterization

The in situ open-cell TEM characterization was conducted using a nanobattery-like configuration with LNO as the working electrode, Li as the reference, and Li_2O as the solid electrolyte. All the in situ electrochemical tests were conducted in a JEOL 2100Plus TEM operated at 200 kV with the open-cell holder (PicoFemto, Zeptools Technology, China). To assemble the nanobattery, the holder was moved into an Ar-filled glovebox. The LNO cathode material was in powder form, which was transferred onto a half-holey carbon copper grid, while the Li metal was scratched on the tip of a tungsten needle. The holder was then transferred to the microscope column within a sealed Ar-filled bag. The Li metal was later moved toward the LNO NPs inside the TEM. After contact, a positive bias was applied to the half-cell to trigger and drive the delithiation process. This process was recorded by the CCD camera (Gatan's K3) of the TEM. Further microstructure and element distribution within powder samples were investigated by high angle annular DF (HAADF) STEM. The images were collected using an aberration-corrected (Cs) TEM/STEM JEOL 2100FCs microscope operating at 200 kV equipped with a Gatan GIF Quantum SE for EELS. STEM/EELS spectra and maps were using an 8.3 mrad convergence angle and a 0.25 eV/channel. The measurements of lattice spacing recorded in HRTEM micrographs were made using digital image analysis of reciprocal space parameters. The analysis was carried out by the Digital Micrograph software. To quantify the intensity ratio of Ni L_3/L_2 peaks, first the noise background of the spectrums was extracted and the NLLS/Gaussian peak fitting of each Ni peak L_2 and L_3 was also conducted. The phase and orientation maps were determined by comparing and matching each diffraction pattern in the collected 4D-STEM dataset. 4D-STEM experiments were carried out using a Tescan Tensor operated at 100 kV in a regular nanobeam diffraction setup and data was acquired using a DECTRIS QUADRO detector. The acquired 4D datasets were

processed using the py4DSTEM package, allowing for the extraction of spatially resolved structural and phase information.

Author Contributions

B. Layla Mehdi: conceptualization (lead), formal analysis (lead), funding acquisition (lead), investigation (lead), resources (lead), supervision (lead), writing – original draft (lead), writing – review & editing (lead). **Ioannis Siachos:** conceptualization (lead), data curation (lead), formal analysis (lead), investigation (lead), methodology (lead), visualization (lead), writing – original draft (lead), writing – review & editing (lead). **Xiaodong Liu:** data curation (equal), formal analysis (equal), methodology (equal). **Weiqun Li:** formal analysis (supporting), methodology (supporting). **Amirafshar Moshtaghpour:** data curation (equal). **Annalena R. Genreith-Schriever:** conceptualization (equal), formal analysis (equal), supervision (equal). **Tingting Yang:** data curation (equal), funding acquisition (equal), investigation (equal). **Penghan Lu:** supervision (equal). **Rafal E. Dunin-Borkowski:** supervision (supporting). **Clare P. Gray:** supervision (supporting).

Acknowledgments

This work was supported by the Faraday Institution [FIRG024] through the Degradation Project. The authors thank the Ernst Ruska-Research Centre for granting us access to the Microscopy and Spectroscopy Facility (ER-C-1) to perform part of this work. The author gratefully acknowledges the Albert Crewe Centre for Electron Microscopy at University of Liverpool, UK.

Funding

This work was supported by the Research England (EP/X03769X/1); Faraday Institution (EGR10913).

Conflicts of Interest

The authors declare no conflicts of interest.

Data Availability Statement

The data that support the findings of this study are available from the corresponding author upon reasonable request.

References

1. N. Nitta, F. Wu, J. T. Lee, and G. Yushin, "Li-Ion Battery Materials: Present and Future," *Materials Today* 18 (2015): 252–264.

2. A. Manthiram, "A Reflection on Lithium-Ion Battery Cathode Chemistry," *Nature Communications* 11 (2020): 1550.

3. J. Xu, F. Lin, M. M. Doeff, and W. Tong, "A Review of Ni-Based Layered Oxides for Rechargeable Li-Ion Batteries," *Journal of Materials Chemistry A* 5 (2017): 874–901.

4. M. D. Radin, S. Hy, M. Sina, et al., "Narrowing the Gap between Theoretical and Practical Capacities in Li-Ion Layered Oxide Cathode Materials," *Advanced Energy Materials* 7 (2017): 1602888.

5. C. Xu, P. J. Reeves, Q. Jacquet, and C. P. Grey, "Phase Behavior during Electrochemical Cycling of Ni-Rich Cathode Materials for Li-Ion Batteries," *Advanced Energy Materials* 11 (2021): 2003404.

6. S. Ahmed, M. Bianchini, A. Pokle, et al., "Visualization of Light Elements Using 4D STEM: The Layered-to-Rock Salt Phase Transition in $LiNiO_2$ Cathode Material," *Advanced Energy Materials* 10 (2020): 2001026.

7. L. de Biasi, A. Schiele, M. Roca-Ayats, et al., "Phase Transformation Behavior and Stability of $LiNiO_2$ Cathode Material for Li-Ion Batteries Obtained from In Situ Gas Analysis and Operando X-Ray Diffraction," *ChemSusChem* 12 (2019): 2240–2250.

8. C. Delmas, C. Fouassier, and P. Hagenmuller, "Structural Classification and Properties of the Layered Oxides," *Physica B+C* 99 (1980): 81–85.

9. I. D. Seymour, S. Chakraborty, D. S. Middlemiss, D. J. Wales, and C. P. Grey, "Mapping Structural Changes in Electrode Materials: Application of the Hybrid Eigenvector-Following Density Functional Theory (DFT) Method to Layered $Li_{0.5}$ MnO_2," *Chemistry of Materials* 27 (2015): 5550–5561.

10. C. M. Wang, W. Xu, J. Liu, et al., "In Situ Transmission Electron Microscopy and Spectroscopy Studies of Interfaces in Li Ion Batteries: Challenges and Opportunities," *Journal of Materials Research* 25 (2010): 1541–1547.

11. T. Ohzuku, A. Ueda, and M. Nagayama, "Electrochemistry and Structural Chemistry of LiNiO2 (R3m) for 4 Volt Secondary Lithium Cells," *Journal of the Electrochemical Society* 140 (1993): 1862–1870.

12. C. Delmas, J. P. Pérès, A. Rougier, et al., "On the Behavior of the LixNiO2 System: an Electrochemical and Structural Overview," *Journal of Power Sources* 68 (1997): 120–125.

13. J. R. Dahn, U. von Sacken, and C. A. Michal, "Structure and Electrochemistry of Li1±yNiO2 and a New Li2NiO2 Phase with the Ni (OH)2 Structure," *Solid State Ionics* 44 (1990): 87–97.

14. E. McCalla, G. Carey, and J. R. Dahn, "Lithium Loss Mechanisms during Synthesis of Layered LixNi2−xO2 for Lithium Ion Batteries," *Solid State Ionics* 219 (2012): 11–19.

15. Y. Koyama, H. Arai, I. Tanaka, Y. Uchimoto, and Z. Ogumi, "Defect Chemistry in Layered Li M O_2 (M = Co, Ni, Mn, and $Li_{1/3}$ $Mn_{2/3}$) by First-Principles Calculations," *Chemistry of Materials : A Publication of the American Chemical Society* 24 (2012): 3886–3894.

16. J. Cen, B. Zhu, and D. O. Scanlon, "Exploring Battery Cathode Materials in the Li-Ni-O Phase Diagrams Using Structure Prediction," *Journal of Physics: Energy* 5 (2023): 035005.

17. J. Reed, G. Ceder, and A. Van der Ven, "Layered-to-Spinel Phase Transition in Li[sub x]MnO[sub 2]," *Electrochemical and Solid-State Letters* 4 (2001): A78–A81.

18. S. Kim, X. Ma, S. P. Ong, and G. Ceder, "A Comparison of Destabilization Mechanisms of the Layered NaxMO2 and LixMO2 Compounds upon Alkali De-Intercalation," *Physical Chemistry Chemical Physics : Pccp* 14 (2012): 15571–15578.

19. X. Wu, S. Li, B. Yang, and C. Wang, "In Situ Transmission Electron Microscopy Studies of Electrochemical Reaction Mechanisms in Rechargeable Batteries," *Electrochemical Energy Reviews* 2 (2019): 467–491.

20. P. Harks, F. Mulder, and P. Notten, "In Situ Methods for Li-Ion Battery Research: A Review of Recent Developments," *Journal of Power Sources* 288 (2015): 92–105.

21. Z. Chen, Q. Wang, and K. Amine, "Understanding the Stability of Aromatic Redox Shuttles for Overcharge Protection of Lithium-Ion Cells," *Journal of the Electrochemical Society* 153 (2006): A2215–A2221.

22. C.-M. Wang, "In Situ Transmission Electron Microscopy and Spectroscopy Studies of Rechargeable Batteries under Dynamic Operating Conditions: A Retrospective and Perspective View," *Journal of Materials Research* 30 (2015): 326–339.

23. C. Shen, C. Li, R. Huang, et al.," Eco-friendly p-type Cu2SnS3 thermoelectric material: crystal structure and transport properties,"*Scientific Reports* 6 (2016): 1–11.

24. Y. S. Meng, G. Ceder, C. P. Grey, et al., "Cation Ordering in Layered O3 $Li[Ni_x$ $Li_{1/3-2x/3}$ $Mn_{2/3-x/3}]O_2$ ($0 \le x \le {}^1/_2$) Compounds," *Chemistry of Materials* 17 (2005): 2386–2394.

25. J. Y. Huang, L. Zhong, C. M. Wang, et al., "In Situ Observation of the Electrochemical Lithiation of a Single SnO_2 Nanowire Electrode," *Science (new York, N.y.)* 330 (2010): 1515–1520.

26. M. M. Islam, M. T. Alam, T. Okajima, and T. Ohsaka, "Electrical Double Layer Structure in Ionic Liquids: An Understanding of the Unusual Capacitance−Potential Curve at a Nonmetallic Electrode," *The Journal of Physical Chemistry C* 113 (2009): 3386–3394.

27. C. Gong, S. Pu, A. W. Robertson, *In Advances in Sustainable Energy: Policy, Materials and Devices*. 545–596 (Elsevier, 2021).

28. R. F. Egerton, "Control of Radiation Damage in the TEM," *Ultramicroscopy* 127 (2013): 100–108.

29. S. K. Eswaramoorthy, J. M. Howe, and G. Muralidharan, "In Situ Determination of the Nanoscale Chemistry and Behavior of Solid-Liquid Systems," *Science (new York, N.y.)* 318 (2007): 1437–1440.

30. A. R. Genreith-Schriever, H. Banerjee, A. S. Menon, et al., "Oxygen Hole Formation Controls Stability in LiNiO2 Cathodes," *Joule* 7 (2023): 1623–1640.

31. S. J. Pennycook, "Z-Contrast Stem for Materials Science," *Ultramicroscopy* 30 (1989): 58–69.

32. Q. Stoyel, F. Voisard, N. Brodusch, G. Demopoulos, and R. Gauvin, "Methods for Simulation of Electron Energy Loss Spectra for Low Energy Edges in Battery Materials," *Microscopy and Microanalysis* 24 (2018): 440–441.

33. M. Saitoh, X. Gao, T. Ogawa, et al., "Systematic Analysis of Electron Energy-Loss Near-Edge Structures in Li-Ion Battery Materials," *Physical Chemistry Chemical Physics : Pccp* 20 (2018): 25052–25061.

34. J. H. Seo and J.-H. Kwon, "Unveiling Oxygen K-Edge and Cobalt L-Edge Electron Energy Loss Spectra of Cobalt Hydroxide and Their Evolution under Electron Beam Irradiation," *Nanomaterials* 13 (2023): 2767.

35. M. Hepting, M. P. Dean, and W.-S. Lee, "Soft X-Ray Spectroscopy of Low-Valence Nickelates," *Frontiers in Physics* 9 (2021): 808683.

36. O. L. Krivanek, M. F. Chisholm, V. Nicolosi, et al., "Atom-by-Atom Structural and Chemical Analysis by Annular Dark-Field Electron Microscopy," *Nature* 464 (2010): 571–574.

37. K. C. Bustillo, S. E. Zeltmann, M. Chen, et al., "4D-STEM of Beam-Sensitive Materials," *Accounts of Chemical Research* 54 (2021): 2543–2551.

38. A. Kobler, C. Brandl, H. Hahn, and C. Kübel, "In Situ Observation of Deformation Processes in Nanocrystalline Face-Centered Cubic Metals," *Beilstein Journal of Nanotechnology* 7 (2016): 572–580.

39. C. Ophus, S. E. Zeltmann, A. Bruefach, et al., "Automated Crystal Orientation Mapping in py4DSTEM Using Sparse Correlation Matching," *Microscopy and Microanalysis* 28 (2022): 390–403.

40. H. Yang, R. N. Rutte, L. Jones, et al., "Simultaneous Atomic-Resolution Electron Ptychography and Z-Contrast Imaging of Light and Heavy Elements in Complex Nanostructures," *Nature Communications* 7 (2016): 12532.

41. W. Song, M. A. Pérez-Osorio, J.-J. Marie, et al., "Direct Imaging of Oxygen Shifts Associated with the Oxygen Redox of Li-Rich Layered Oxides," *Joule* 6 (2022): 1049–1065.

42. I. Siachos, W. Li, C. S. Coates, A. R. Genreith-Schriever, C. P. Grey, and B. L. Mehdi, "In-Situ (S)TEM Investigation of Phase Transformation Mechanism in the Ni-Rich Cathodes During Cycling," *Microscopy and Microanalysis* 28 (2022): 1852–1853.

43. C. Xu, K. Märker, J. Lee, et al., "Bulk Fatigue Induced by Surface Reconstruction in Layered Ni-Rich Cathodes for Li-Ion Batteries," *Nature Materials* 20 (2021): 84–92.

44. A. Rougier, P. Gravereau, and C. Delmas, "Optimization of the Composition of the Li1 − z Ni1 + z O 2 Electrode Materials: Structural, Magnetic, and Electrochemical Studies," *Journal of the Electrochemical Society* 143 (1996): 1168–1175.

45. A. Hirano, R. Kanno, Y. Kawamoto, et al., "Relationship between Non-Stoichiometry and Physical Properties in LiNiO2," *Solid State Ionics* 78 (1995): 123–131.

46. R. Kanno, H. Kubo, Y. Kawamoto, et al., "Phase Relationship and Lithium Deintercalation in Lithium Nickel Oxides," *Journal of Solid State Chemistry* 110 (1994): 216–225.

47. C. S. Yoon, D.-W. Jun, S.-T. Myung, and Y.-K. Sun, "Structural Stability of $LiNiO_2$ Cycled above 4.2 V," *ACS Energy Letters* 2 (2017): 1150–1155.

48. C. Wang, R. Zhang, K. Kisslinger, and H. L. Xin, "Atomic-Scale Observation of O1 Faulted Phase-Induced Deactivation of $LiNiO_2$ at High Voltage," *Nano Letters* 21 (2021): 3657–3663.

49. Z. Wang, D. Santhanagopalan, W. Zhang, et al., "In Situ STEM-EELS Observation of Nanoscale Interfacial Phenomena in All-Solid-State Batteries," *Nano Letters* 16 (2016): 3760–3767.

50. D. Fraggedakis, N. Nadkarni, T. Gao, et al., "A Scaling Law to Determine Phase Morphologies during Ion Intercalation," *Energy & Environmental Science* 13 (2020): 2142–2152.

51. A. J. Merryweather, C. Schnedermann, Q. Jacquet, C. P. Grey, and A. Rao, "Operando Optical Tracking of Single-Particle Ion Dynamics in Batteries," *Nature* 594 (2021): 522–528.

52. P. Bai, D. A. Cogswell, and M. Z. Bazant, "Suppression of Phase Separation in $LiFePO_4$ Nanoparticles During Battery Discharge," *Nano Letters* 11 (2011): 4890–4896.

53. H. Das, A. Urban, W. Huang, and G. Ceder, "First-Principles Simulation of the (Li–Ni–Vacancy)O Phase Diagram and Its Relevance for the Surface Phases in Ni-Rich Li-Ion Cathode Materials," *Chemistry of Materials* 29 (2017): 7840–7851.

54. Q. Li, D. Ning, D. Wong, et al., "Improving the Oxygen Redox Reversibility of Li-Rich Battery Cathode Materials via Coulombic Repulsive Interactions Strategy," *Nature Communications* 13 (2022): 1123.

55. J. G. Lozano, G. T. Martinez, L. Jin, P. D. Nellist, and P. G. Bruce, "Low-Dose Aberration-Free Imaging of Li-Rich Cathode Materials at Various States of Charge Using Electron Ptychography," *Nano Letters* 18 (2018): 6850–6855.

56. R. F. Egerton, *Electron Energy-Loss Spectroscopy in the Electron Microscope* (Springer, 2011).

57. K. J. Carroll, D. Qian, C. Fell, et al., "Probing the Electrode/Electrolyte Interface in the Lithium Excess Layered Oxide Li1.2Ni0.2Mn0.6O2," *Physical Chemistry Chemical Physics : Pccp* 15 (2013): 11128–11138.

58. B. Xu, C. R. Fell, M. Chi, and Y. S. Meng, "Identifying Surface Structural Changes in Layered Li-Excess Nickel Manganese Oxides in High Voltage Lithium Ion Batteries: A Joint Experimental and Theoretical Study," *Energy & Environmental Science* 4 (2011): 2223–2233.

59. C. R. Fell, D. Qian, K. J. Carroll, M. Chi, J. L. Jones, and Y. S. Meng, "Correlation Between Oxygen Vacancy, Microstrain, and Cation Distribution in Lithium-Excess Layered Oxides During the First Electrochemical Cycle," *Chemistry of Materials* 25 (2013): 1621–1629.

60. N. Browning, J. Yuan, and L. Brown, "Real-Space Determination of Anisotropic Electronic Structure by Electron Energy Loss Spectroscopy," *Ultramicroscopy* 38 (1991): 291–298.

61. N. Browning, D. Wallis, P. Nellist, and S. J. Pennycook, "EELS in the STEM: Determination of Materials Properties on the Atomic Scale," *Micron* 28 (1997): 333–348.

62. L. An, J. E. N. Swallow, P. Cong, et al., "Distinguishing Bulk Redox from Near-Surface Degradation in Lithium Nickel Oxide Cathodes," *Energy & Environmental Science* 17 (2024): 8379–8391.

63. P. Batson, "Advanced Spatially Resolved EELS in the STEM," *Ultramicroscopy* 78 (1999): 33–42.

64. P. Batson, "Atomic resolution EELS analysis of a misfit dislocation at a GeSi/Si interface," *Physica B* 273 (1999): 593–597.

65. F. Cosandey, J. F. Al-Sharab, F. Badway, G. G. Amatucci, and P. Stadelmann, "EELS Spectroscopy of Iron Fluorides and FeF_x/C

Nanocomposite Electrodes Used in Li-Ion Batteries," *Microscopy and Microanalysis* 13 (2007): 87–95.

66. G. A. Botton, C. C. Appel, A. Horsewell, and W. M. Stobbs, "Quantification of the EELS near-edge Structures to Study Mn Doping in Oxides," *Journal of Microscopy* 180 (1995): 211–216.

67. C. Colliex, T. Manoubi, and C. Ortiz, "Electron-Energy-Loss-Spectroscopy Near-Edge Fine Structures in the Iron-Oxygen System," *Physical Review B* 44 (1991): 11402–11411.

68. K. Bawane, P. Manganaris, Y. Wang, et al., "Determining Oxidation States of Transition Metals in Molten Salt Corrosion Using Electron Energy Loss Spectroscopy," *Scripta Materialia* 197 (2021): 113790.

69. T. G. Sparrow, B. G. Williams, C. N. R. Rao, and J. M. Thomas, "L3/L2 White-Line Intensity Ratios in the Electron Energy-Loss Spectra of 3d Transition-Metal Oxides," *Chemical Physics Letters* 108 (1984): 547–550.

70. X. Gao, Y. H. Ikuhara, C. A. J. Fisher, et al., "Structural Distortion and Compositional Gradients Adjacent to Epitaxial $LiMn_2$ O_4 Thin Film Interfaces," *Advanced Materials Interfaces* 1 (2014): 1400143.

71. J. Graetz, C. Ahn, R. Yazami, and B. Fultz, "Highly Reversible Lithium Storage in Nanostructured Silicon," *Electrochemical and Solid-State Letters* 6 (2003): A194–A197.

Supporting Information

Additional supporting information can be found online in the Supporting Information section. **Supporting Figure S1:** SEM figures of LNO cathode particles at different magnifications. The secondary particle nature of the material is visible, and an inset OF (b) shows the surface texture in detail. **Supporting Figure S2**: EDS mapping shows a) the electron image of LNO particle, b) elemental composition presented as the wt% of the main elements Ni, O, and other elements appeared from the experimental set-up, c) map of Nickel in green color suggesting that is the main element of the structure and d) map of Oxygen. **Supporting Figure S3**: (a) High-resolution TEM image illustrates clearly the layered structure of the pristine LNO with distinct atomic planes of the (003) facet. (b) Selected area diffraction pattern of TEM image showing the main reflections. The line profile is used to calculate the d-spacing of that facet, which is 4.8 Å (c). **Supporting Figure S4**: (a,b) Time-resolved TEM images of an LNO particle brought into direct physical contact with Li/Li_2O without applied electrical bias, acquired at 1 s and 60 s, respectively. FFTs (insets) confirm preservation of the layered structure with intact (003) reflections. No lattice expansion, phase transition, crystallinity loss, or rock-salt formation is observed. This control demonstrates that neither physical contact nor electron-beam exposure alone induces the transformations reported under applied bias. **Supporting Figure S5**: EELS spectrum taken at the low loss region of $LiNiO_2$, close to the zero-loss peak. 6 spectrums taken within the LNO particle (fig.5). 1 is taken from the surface, 6 from the bulk. **Supporting Figure S6**: Ni L3/L2 intensity of ratio as calculated between three reference samples (NiO for Ni II, LNO for Ni III, and Ni peroxide for Ni IV) and one experimental spectrum taken from the reaction front (red-pink region) of the particle. **Supporting Movie S1**. Low magnification video of the reaction between Li tip and LNO during Li removal when positive voltage is applied. 70 seconds of delithiation led to 26% expansion of the LNO particle. **Supporting Movie S2**. Low magnification video of the reaction between Li^+/Li_2O and LNO during lithium de-intercalation, when positive voltage is applied (4.3V). 60 seconds of delithiation led to 30.6% expansion of the LNO particle. **Supporting Movie S3**. HRTEM video shows the reaction between LNO and Li tip when +4.3V is stored in the battery cathode. The movie shows the phase transition of the (003) atomic planes of LNO into rock-salt (NiO) upon delithiation. **Supporting Movie S4**. HRTEM video showing the dynamic reactions that take place within the LNO particle during Li ions removal process.